Atomistic molecular dynamics study of interface formation: Al on poly(p-phenylene vinylene)

Ronaldo Giro* and Marília J. Caldas
Instituto de Física, Universidade de São Paulo, Caixa Postal 66318, CEP 05315-970 São Paulo SP, Brazil
(Received 26 May 2008; revised manuscript received 3 September 2008; published 15 October 2008)

We model interface formation by metal deposition on the conjugated polymer poly-para-phenylene vinylene, studying direct aluminum and layered aluminum-calcium structures Al/PPV and Al/Ca/PPV. To do that we use classical molecular dynamics simulations, checked by *ab initio* density-functional theory calculations, for selected relevant configurations. We find that Al not only migrates easily into the film, with a strong charge transfer to the neighboring chains, but also promotes rearrangement of the polymer in the interfacial region to the hexagonal structure. On the other hand, our results indicate that a thin Ca layer is sufficient to protect the film and maintain a well-defined metal/polymer interface, and that also a thin Al capping layer may protect the whole from environmental degradation.

DOI: 10.1103/PhysRevB.78.155312 PACS number(s): 68.43.−h, 68.55.−a, 82.65.+r, 85.60.Jb

I. INTRODUCTION

The use of conjugated polymer films in the active section of optoelectronic devices is extremely interesting as a route for new technologies,[1] with several advantages over conventional materials as regards weight and flexibility, and could be optimal for large-area displays and other applications. One of the crucial issues is to balance charge injection through hybrid interfaces,[2] since the systems are composed of the organic films and inorganic electrodes, usually oxides for the anode and metals for the cathode. One usual architecture for polymer light-emitting devices (PLEDs) is vertical, metal/polymer/oxide, and balanced charge injection at both ends depends primarily on the difference in work function of the layers. The work-function issue at the anode can be solved, as for conventional LEDs, by step-grading the interfaces on the polymer side.[2,3] At the cathode interface the problem is even more serious due to the very low work function of many polymers, so that, e.g., for the aluminum/poly-*para*-phenylene-vinylene (Al/PPV) interface we would have a Schottky junction.[4] A better match would be achieved through use of calcium as the metal cathode, since it is a low-work-function metal. Calcium is very reactive and presents low environmental stability, and an often employed grading at the cathode is then the use of Ca directly in contact with the polymer, capped by other metals.[5,6] In the case of Al/Ca/PPV structuring, the overall device performance has been found[5] to be the same as for a pure Ca/PPV structure, already for a thin Ca layer of ca. 2 Å. This was attributed by the authors[5] to Ca doping of the PPV polymer; however, in a previous work,[7] we have shown that PPV doping should not be expected in the case of Ca, so that this strong beneficial effect has probably a different origin.

Another point to be investigated is the atomistic and electronic structure of the hybrid interface. Here it is crucial that the minimum density of traps should be present. One of the usual techniques for building vertical-architecture devices is to evaporate the metal (cathode) on top of the polymer layer,[8–10] and thus it would be of strategic relevance to have a closer understanding of the process of interface formation, since the deposition process itself could be responsible for introduction of defective interfacial regions, with damaging effect.

In our previous Rapid Communication[7] we have shown that the Ca/PPV interface is very robust, as long as unsubstituted PPV polymer chains are used. Our focus here is on the behavior of Al on PPV, and on the capped interface Al/Ca/PPV.

It is widely accepted that polymer films are mainly structured as ordered quasicrystalline grains immersed in amorphous regions, as recently shown[11] for poly[2-methoxy-5-(2′-ethyl-hexyloxy)-1,4-phenylene vinylene] (MEH-PPV). As for pure nonsubstituted PPV, the polymer is known[12] to form crystalline herring-bone aggregates and we may expect to see, at the film surface, domains with crystalline arrangement in different expositions, embedded in disordered domains. As such, the atomistic study of metal deposition on different exposed crystalline surfaces brings important information on the interface formation/degradation mechanisms. We study here, as in our previous work for Ca/PPV, Al deposition on three different crystalline surfaces of PPV: the two "closed" orientations (100) and (010), and the "open" (001) surface (see Fig. 1). Furthermore, to approach layered structures, we simulate Al deposition on top of the Ca/(010)PPV system.

Our study is based on classical molecular dynamics (CMD) to describe the deposition process and the evolution of the system, at room temperature. CMD is known to describe quite well the geometrical structure of supramolecular aggregates, and is well established for different materials in more than one parametrization scheme. We here adopt the universal force field (UFF), treating charge redistribution through the charge equilibration scheme,[13,14] and with a special parametrization we adapted from Ref. 15 for the metal atoms. The deposition process is simulated by impact molecular dynamics (IMD) at a given temperature. For selected configurations we perform also *ab initio* calculations, focusing on the charge of the metal atoms, within density-functional theory (DFT) formalism.

We find that direct deposition of Al on PPV presents completely different characteristics when compared to Ca. Our results show migration of Al into the first subsurface layer, with rearrangement of the polymer chains to hexagonal arrangement, already for the closed surfaces; structural disorder on the polymer side in these cases reaches the third bilayer. Furthermore, we find for the embedded Al atoms a

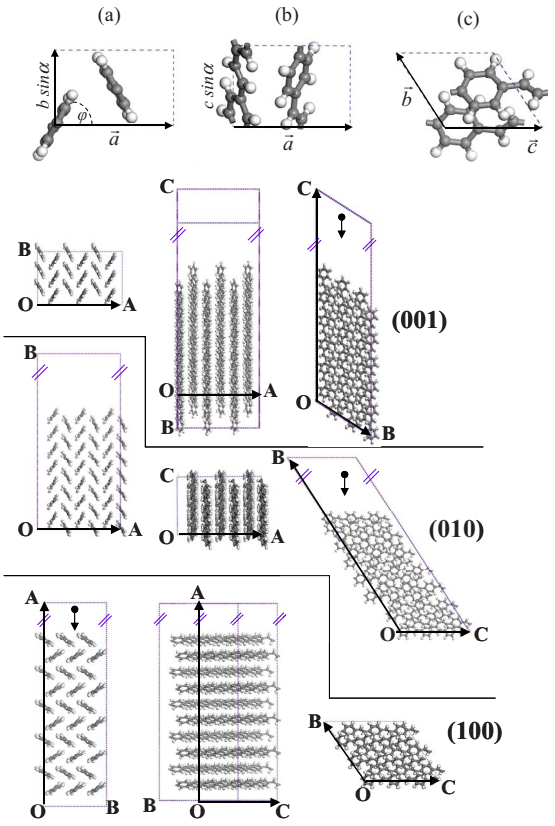

FIG. 1. (Color online) Schematic projected PPV unit cell in the (a) (001), (b) (100), and (c) (010) directions. The cell parameters are taken from Ref. 12: $a=7.9$, $b=6.05$, and $c=6.54$ Å with $\alpha=123°$, $\beta=\gamma=90°$. The setting angle φ is between 56 and 68°. In the lower panels we show the simulation models for the three PPV surface studied in this work, viewed from different angles. We indicate the supercell axis, and also the direction adopted for the initial velocity of the deposited metal atoms.

strong charge transfer, which may characterize doping of the polymer film. Moving to the behavior of Al deposited on the Ca/(010)PPV system, we find that a minimum thickness of the Ca layer is necessary to preserve the ordering of the metal film. On the other hand we see that, even for very thin Ca layers, Al atoms do not reach the polymer film indicating there is effective protection of the organic/metal interfacial layer.

II. METHODOLOGY

We have carried out CMD simulations based on the well-established standard molecular force field UFF.[13] The UFF has been parametrized for the full Periodic Table, and is very reliable for the description of geometrical and structural properties for molecular systems, thus results for PPV are quite satisfactory, in isolated and condensed forms. However, this particular parametrization was not meant for bulk metals, and since our study is focused on interfaces between metal and polymer, it was necessary to develop a specific force field. To do that, we based our parametrization on the work by T. Halicioğlu and Pound.[15] These authors developed a simple method to estimate parameters for the Lennard-Jones (LJ) 6-12 pair potentials using crystalline state properties at any given temperature. This is very important since the parameters for the interactions between metal atoms are generally calculated[16] from crystalline state physical properties (such as cohesive energy, compressibility, lattice constant, etc.) extrapolated to 0 K, while experimental values for physical properties near $T=0$ K are sometimes difficult to find. As can be seen in Table III of the Appendix, our LJ force field describes bulk crystalline geometrical properties—lattice parameters and angles—for Al and Ca at room temperature in different allotropic phases, while for phase transitions and properties at high pressures we found that a Morse-type potential produces more reliable results. Since here we are treating room-pressure phenomena we are everywhere using LJ potentials for Al and Ca; however, we include in the Appendix parameters for Na, Al, Ca, Ag, and Au both for the LJ and Morse implementations.

We use thus the standard UFF parametrization for PPV, while nonbonded interactions between metal atoms, and metal and polymer-chain atoms are treated by LJ and electrostatic terms; our parametrization for the LJ term is included through the Open Force Field (OFF) module within CERIUS2.[21] When calculating the electrostatic interaction we adopt charges calculated through the equilibration (QEq) procedure in Ref. 22 which we reproduce below for clarity. The QEq is a general scheme proposed for predicting the evolution of charges in molecular systems, which relies on the expansion of the total energy

$$E(Q) = E_0 + Q\left[\frac{\partial E}{\partial Q}\right]_0 + \frac{1}{2}Q^2\left[\frac{\partial^2 E}{\partial Q^2}\right]_0. \tag{1}$$

We can write, in terms of the ionization potential IP and electron affinity EA for the atom,

$$\chi^0 = \left[\frac{\partial E}{\partial Q}\right]_0 = \frac{1}{2}(\mathrm{IP}+\mathrm{EA}); \quad V^0 = \left[\frac{\partial^2 E}{\partial Q^2}\right]_0 = \mathrm{IP}-\mathrm{EA}, \tag{2}$$

and for a polyatomic system we have

$$E(1,\ldots,N) = \Sigma_I\left[E_{I0} + \chi_I^0 Q_I + \frac{1}{2}V_I^0 Q_I^2\right] + \Sigma_{I<J} Q_I Q_J V_{IJ},$$

$$\chi_I(1,\ldots,N) = \frac{\partial E}{\partial Q_I} = \chi_I^0 + V_I^0 Q_I + \Sigma_{J\neq I} V_{IJ} Q_J,$$

where V_{IJ} is the Coulomb interaction between atoms I,J. The charge on each atom Q_A is then iteratively solved, for a given geometric configuration of the system, as a function of all the other atomic charges through equilibrating the "atomic scale chemical potential"

$$\chi_1 = \chi_2 = \cdots \chi_N, \tag{3}$$

with the fixed total charge as a constraint; the main parameters are based only on experimental atomic properties, with additional constraints given by the allowable valence-charge variation and special approximations for small atomic separations.

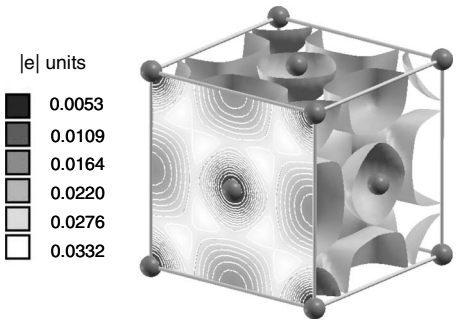

FIG. 2. Charge density for metallic aluminum in the bulk obtained from DFT-LDA electronic structure calculation, emphasizing the "basinlike" character of the charge density. Charge density was plotted with XCRYSDEN package (Refs. 27 and 28).

In our case, where we have a compact metal film in close contact with the polymer surfaces, the QEq procedure represents an efficient way of taking into account the electronic influence on the system evolution. However, we must clearly be careful to test results,[23] especially in our case where we need to get a sound picture of doping and charge transfer. To do that, we extract smaller sections of the relevant configurations obtained by the CMD technique, and obtain the electronic structure by *ab initio* DFT calculations using the ABINIT package.[24] We focus on Bader charges,[25,26] which are directly related to the charge density distribution $\rho(\mathbf{r})$ for the complete system.

In the Bader partition, to obtain the charge of an atom, the space is divided by surfaces that run through minima in the charge density $\nabla\rho=0$ (such regions are usually named *Bader basins*). In this way, the Bader charge Q_A for atom A is obtained through the integration of the electronic density inside the corresponding Bader basin Ω, as

$$Q_A = Z_A - \int_{\Omega} \rho(\mathbf{r}) d\mathbf{r}, \tag{4}$$

where Z_A is the atomic number.

The Bader charge procedure is very reliable to predict charges for metals, where it is easy to determine the surfaces that run through minima in the charge density (as we show in Fig. 2 for Al in the face-centered-cubic structure), so it is well suited to our work here, since we are focusing exactly on the charge on metal atoms near the interface with PPV. We model the crystalline polymer surfaces through the slab configuration usually adopted to study extended surfaces of inorganic compounds, that is, as two-dimensional (2D)-infinite slabs of a chosen orientation of the "bulk" material, and a chosen width in the third direction, separated by vacuum regions of adequate depth, with periodic boundary conditions in the three directions. The herring-bone primitive cell parameters for PPV were taken from Ref. 12. Having established the number of polymer (or monomer) layers and lateral dimensions for each surface, we build supercells separating the slabs by a minimum of 40 Å vacuum, and fully relax the atomic coordinates through classical molecular mechanics (MM) with UFF keeping the supercell parameters fixed. We have, respectively, the equivalent to $3\times3\times6$ polymer unit cells for the (001) surface supercell, $3\times7\times3$ for (010), and $5\times3\times3$ for (100). This corresponds to a minimum of five bilayers, in this last case, of polymer chains in the surface simulation cell. The chosen supercells, with the relaxed configurations, are shown in detail in Fig. 1. Our simulations involve from 1478 atoms, for the smallest cell of the clean (001)PPV surface, to 3350 atoms in the case of the capped Al/Ca/PPV system.

We want to simulate metal cathode deposition over the polymer film by thermal evaporation of the metal, for example, from a tungsten boat.[5] To do that, we employ IMD: Five metal atoms are randomly placed at ~15 Å from the surface, and given an initial velocity (of 5 Å/ps for Al and 4 Å/ps for Ca atoms) directed at the surface. MD is then carried out for 10 ps at 300 K in a number-volume-energy (NVE) ensemble. In the middle of this cycle, i.e., at 5 ps, we apply the charge equilibration procedure QEq. The cycle MD-QEq is repeated until enough Al or Ca atoms were deposited. Finally, MD cycles are performed for another 100 ps, at 300 K, in a number-volume-temperature (NVT) ensemble, and during this last part of simulation QEq is calculated at intervals of 10 ps.

In the MM simulations, the following convergence criteria were used: maximum force of 5×10^{-3} kcal/mol Å, root-mean-square (RMS) deviations of 10^{-3} kcal/mol Å, energy differences of 10^{-4} kcal/mol, maximum atomic displacement of 5×10^{-5} Å, and RMS displacement of 10^{-5} Å. In all MD simulations we used time steps of 1 fs. Our DFT calculations are carried out with plane-wave expansions, and local-density approximation (LDA) (Ref. 29) with Teter-Pade parametrization for the exchange-correlation functional[30] together with norm-conserving pseudopotentials[31] for the core electrons using the ABINIT code.[24]

III. RESULTS AND DISCUSSION

In this section, we first detail our results for Al deposition on the three crystalline surfaces of PPV, and then describe the study of Al layered on Ca/PPV.

A. Al/PPV interfaces

We start with the description of Al deposition on the open (001) surface: Although we expect this configuration to be less probable at the free surface, we also clearly expect that, among the crystalline expositions, it will be the most susceptible to migration of metal atoms into the film. Indeed, we found that in this configuration the PPV surface is able to absorb Al atoms by transforming locally to a hexagonal arrangement. A similar configuration has been detected experimentally for PPP and PPV films doped with Na, which stabilize in the hexagonal phase.[32,33] For comparison, we have also simulated deposition of Na on the (001) PPV surface, and our results are shown grouped together in Fig. 3 for the initial steps of deposition. Our results predict the same transformation for deposition of both metals, although more clearly defined in the case of the group-I metal. At these initial stages, migration into the PPV film for both Al and Na does not proceed deeper than ~10 Å.

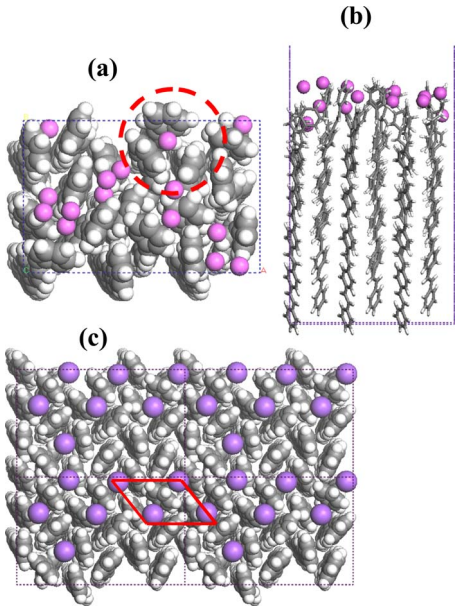

FIG. 3. (Color online) Initial steps of deposition of Al and Na metal atoms on the PPV(001) surface. In (a) and (b) are the top and side views of the Al/PPV cell, and in (c) is the top view of the Na/PPV cell. We highlight in (a) the rearrangement of the local configuration, with the polymer chain ends encapsulating an Al atom; in (c) for the Na deposition the rearrangement is more clearly seen, leading to a quasihexagonal configuration at the surface region.

Continuing the process of Al deposition, we see formation of metal clusters on the surface, until (after ca. 150 ps of deposition) a homogeneous film configuration is reached. When we arrive at 190 ps of simulation we can already identify small crystalline domains, with fcc arrangement, which play an important role in the subsequent organization. As more Al atoms are added, and the CMD simulations are performed, these grains grow and propagate the crystalline arrangement to almost the entire metal structure with, however, still some dislocation defects present at 360 ps of CMD simulation.

On the polymer side of the interface we see disorder due to Al migration down to around 20 Å; after that we recapture the bulk configuration for PPV. Since in our simulation we keep the lateral cell dimensions fixed, there is no free space available for the lattice expansion needed for full phase transformation to hexagonal lattice on the polymer side, which may artificially hinder Al diffusion. However, we already clearly see that Al atoms will migrate more easily than Ca, for which we have seen no migration at all for the same open surface.[7]

We pass now to our results for the closed surfaces starting with the (010) (middle panel of Fig. 1). At the very initial steps of the deposition process, shown in Fig. 4, the grooves of the ordered surface along the chain axis receive the metal atoms resulting in a sparse linear organization. However, already at 30 ps of simulation we see a strong rearrangement of the intermolecular structure for the top polymer chains, leading to encapsulation of Al atoms in hexagonal channels along the chain direction. After this, these metal atoms continue to be embedded to the end of our simulation process (340 ps), while at the free surface we see first the nucleation of Al clusters (seen already in Fig. 4, 50 ps) followed by complete coverage, and finally reorganization of the metal layer to form grains in the crystalline fcc phase. The interfacial layer on the polymer side reaches in this case ca. 15 Å.

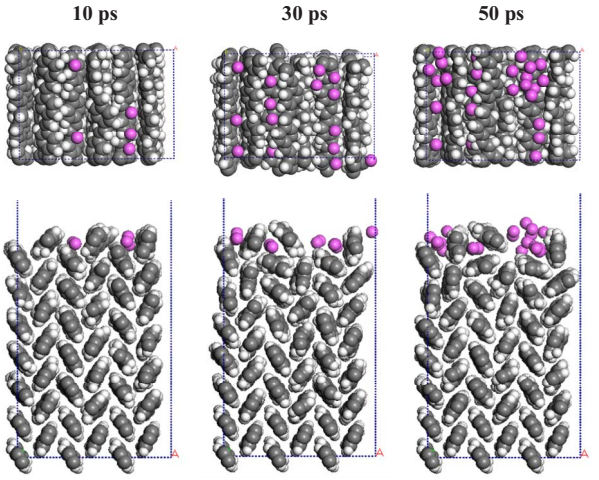

FIG. 4. (Color online) Top and side views of the initial steps of the deposition process for Al on PPV(010). We can see the reorganization of the first surface layer to the hexagonal phase, encapsulating Al atoms.

The same mechanism of metal encapsulation is seen for the (100) surface, as we show in Fig. 5, at the final stage (310 ps) of simulations for Al deposition. Even thus, for this interface we see very little disorder on the polymer side, with the deposition process affecting just the first PPV bilayer (around 6 Å) and after that we recover the crystalline herring-bone arrangement. It is interesting to note that on the metal side of the interface the Al atoms are again in fcc configuration. One way to confirm these findings is by analyzing the pair correlation function [also referred to as radial distribution function[34] or $g(r)$] for the metal atoms. To do

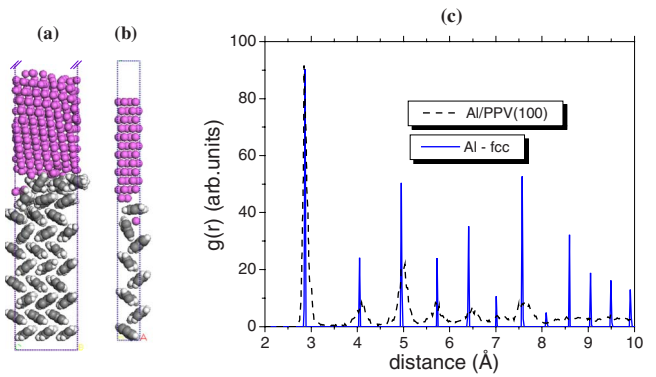

FIG. 5. (Color online) Al deposition on the PPV(100) surface: (a) Representation of the final stage of CMD simulation, viewed from the side; (b) smaller section extracted for *ab initio* calculations of atomic charges; (c) radial distribution functions for Al interatomic distance on this interface configuration (dashed black line) and for bulk Al in the fcc phase, as obtained by our CMD method (solid blue line).

that, we use our optimized lattice parameters for bulk Al in bcc, fcc, and hcp configuration, obtained through MM geometrical optimization when performing our parametrization for the force field (Table II in the Appendix). We then compare the $g(r)$ for Al atoms on the Al/PPV(100) interface, shown also in Fig. 5, with the $g(r)$ obtained for the bulk crystalline configurations. The only situation where the peaks present close agreement is for the fcc arrangement (shown in the figure). The comparative analysis of the $g(r)$ allows us to extract an estimate for the grain radius of ca. 6–8 Å, or (minimum) up to third-nearest-neighbor distance. The broadening of the $g(r)$ peaks in the case of the deposited layer is to be expected, since we have crystalline grains and disordered regions; however, the agreement for the first four peaks is very good, while from 8 Å onward correlation is completely lost. This same methodology applied to the Al/PPV(010) interface leads to similar results.

In any of these systems [Al/PPV (001), (010) and (100)], the calculated charge transfer from Al to PPV is very strong. In electronic charge units, the charge of Al atoms exactly at the metal/polymer interface, on the metal-film side, varies from $Q=+0.2e$ to $Q=+0.5e$, while for the embedded atoms in the (010) and (100) interfaces, or in-diffused in the case of the (001) interface, the charge reaches $Q=+1.0e$. We check our results in this case through *ab initio* calculations for Bader charges for the (smaller) section extracted from the (100) interface illustrated in Fig. 5(b). The charge thus obtained for Al atoms at the interface is $Q=+0.2e$, while for the encapsulated Al atoms the charge amounts to $Q=+0.7e$, in reasonably good agreement with the QEq values. This result is very similar, again, to the behavior of Na for which we have found[7] charge transfer of $Q=(+0.89\pm0.02)e$ and $+1.0e$ through quantum and QEq calculations, respectively. We see that charge equilibration (QEq) charges are always larger than Bader charges, which is expected since the former are taken from experimental and theoretical parameters more in keeping with Lowdin charges.[22]

Our results for the distance between Al and vinylene-C atoms are around 2.87 Å [rising to ~3.15 Å when we do not consider QEq, which we tested for the case of the PPV(010) surface]. These values are larger than that (2.10 Å) obtained with *ab initio* HF/3–21G for PPV dimers reacting with Al in vacuum;[38] this is probably due to the soft-matter-type channel encapsulation, and in fact when we optimize the atomic positions of a smaller section of our cell [similar to that shown in Fig. 5, now for the (010) interface] with DFT within local-density approximation we obtain a value of 2.42 Å, that is, also larger than the value obtained in the vacuum situation. Our results thus do not support the premise[39] that Al atoms in PPV condensed films react with the polymer chain, breaking the conjugation at the vinylene segment.

B. Al/Ca/PPV(010) interfaces

As described in our previous work, Ca deposition on any of the crystalline surfaces of PPV does not lead to metal migration into the film, and at the same time we recover reasonably ordered films after few angstroms on either side of the interface, both for the polymer and metal. We selected particular stages of the deposition process of Ca on the PPV(010) closed surface to simulate the step-graded Al/Ca/PPV interface. We show here results for two distinct cases, with a Ca layer of 10 and 20 Å before initiating the Al deposition. Our minimal width of 10 Å is chosen so as to obtain an initially ordered Ca layer (with less than 10 Å the Ca atoms are still totally disordered even before the deposition of Al atoms).

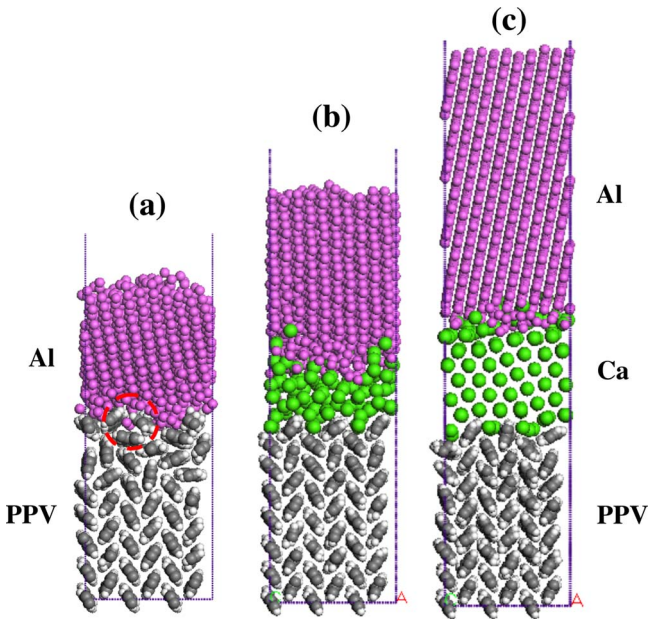

FIG. 6. (Color online) Geometrical features obtained (a) after 340 ps of MD simulations of Al deposition on the clean PPV(010) surface, highlighting the embedded Al atom; (b) after 320 ps of Al deposition on the Ca(10 Å)/PPV(010) structure; and (c) after 350 ps of Al deposition on the Ca(20 Å)/PPV(010) structure.

We show in Fig. 6 for comparison side views for the pure Al deposition process, and for the final stage of the deposition process of Al atoms on the two Ca layers of different thicknesses. We see that for the thinner layer, the impact of the lighter Al atoms brings disorder to the whole of the Ca film, but anyhow already this Ca thickness is enough to block the migration of Al atoms to the PPV interface. We see diffusion and intermixing of Al and Ca atoms, with a disordered interfacial metal layer of ca. 6 Å. Now, confirming this estimate of the interlayer mixing, for the 20 Å Ca layer we find that a region of about 13 Å above the PPV(010) surface remains ordered, as shown also in the same figure.

For all of these structures, after the final steps of simulation the film of Al atoms shows fcc configuration. Also for pure Ca deposition, we had found[7] the metal atoms in fcc configuration. We show in Fig. 7 the analysis of the radial distribution function of metal atoms for the pure Ca deposited film, and for Ca and Al atoms in the composite structure of the thicker Ca interlayer.

IV. SUMMARY AND CONCLUSIONS

In brief, the simulation results for Al deposition on ordered PPV surfaces show always that the metal atoms tend to

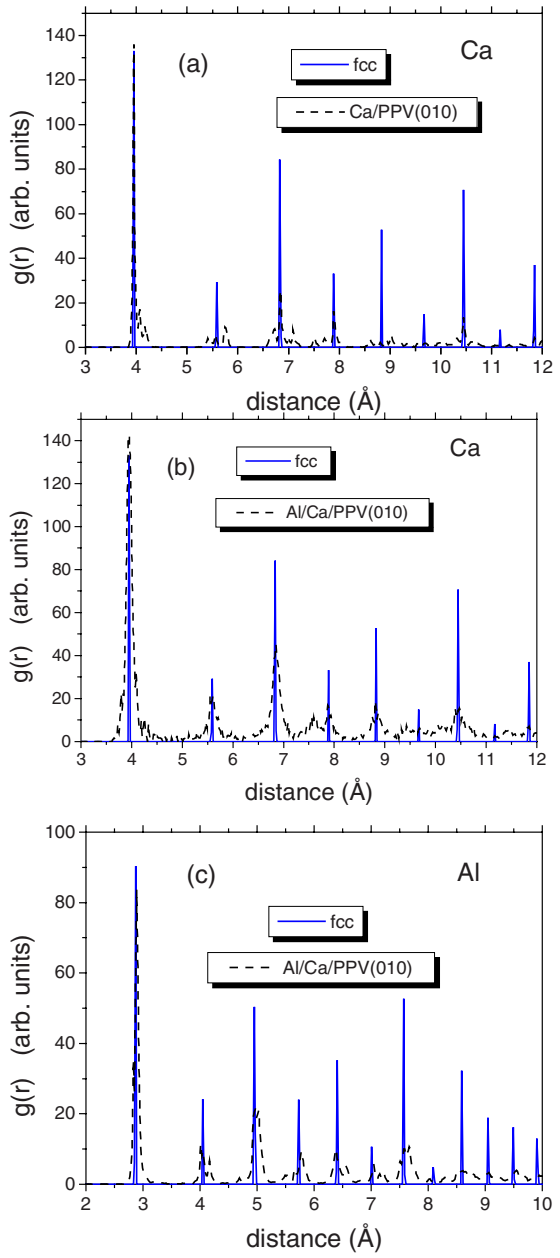

FIG. 7. (Color online) Pair correlation function $g(r)$ for (a) Ca atoms in the pure Ca/PPV(010) structure described in Ref. 7, and (b) in the composite structure of Al/Ca(20 Å)/PPV(010); also for the same structure, in (c) the distribution function for Al atoms. In all frames, the solid lines correspond to the bulk crystalline fcc phase, and the dashed lines to the deposited films.

migrate into the film, and that in the affected region of the film the chains tend to rearrange to the hexagonal phase. Furthermore, for the embedded Al atoms the results show strong charge transfer to the polymer chains, with numbers in reasonable agreement with our *ab initio* calculations. Since both charge transfer and structural rearrangement are very close to those we find for Na, this would indicate doping of the polymer film in the interfacial region.

We remark that in a realistic situation we would also have amorphous regions and grain boundaries[7] at the surface, and this would not only offer more opportunities for atom migration, but also provide more freedom of movement to surface segments of these same crystalline grains. In the case of Al deposition, we reason this will allow for migration much deeper into the film, as indeed found experimentally.[9,39] These results depict thus a scenario for direct Al/PPV interfaces with poor spatial definition, and high probability of deep trenches of metal atoms into the polymer film.

Our results for the layered structures Al/Ca/PPV, on the other hand, stress the robustness of the interface Ca/PPV, which continues to be well defined and preserves order on the polymer side, already for thin Ca layers, we estimate on the order of ~6 Å. On the other hand, when we reach a thickness of another ~6 Å of capping Al, we also will have a robust protection of the Ca film against environmental damage. In conclusion, we find that the primary cause for the beneficial effects of the use of the layered structure resides in the good interfacial properties of the Ca/PPV system, and also on the good resistance of the Ca film to Al migration.

ACKNOWLEDGMENTS

This work was supported in part by the Brazilian agencies CNPq, IMMP/MCT, CAPES, and FAPESP. We are thankful for the use of the computer facilities at LCCA-USP.

APPENDIX: FORCE FIELD DEVELOPMENT

We report here the values we use for the long-range parameters needed to include the dispersion interactions in the interatomic potentials used in the molecular mechanics and molecular dynamics (MD) simulations. We have obtained parameters for Na, Ca, Ag, Au and Al, and all metal-metal and metal/PPV interactions are modeled by electrostatic and dispersion interactions. We include our special parametrization using the OFF module from CERIUS2 software package[21] with the universal force field parametrization from Ref. 13 for all other interactions; that is for PPV/PPV chains, the interactions are modeled by electrostatic, Lennard-Jones (6-12), bond stretch, bond angle bend, and torsional rotational terms.[13,40] As for any classical force field, we have to define atom types for each element according to the hybridization environment, and in our case new types of metal atoms were included to differentiate from metals in coordination compounds.

1. Low pressure: LJ-6-12 for E_{vdw}

In the studies for the interfaces reported here, at room pressure, we use the Lennard-Jones (6-12) potentials as defined in the following equation, for atoms i of type I and j of type J:

$$E_{vdw}^{\mathrm{LJ}} = D_{IJ}\left[\left(\frac{r_{IJ}}{R_{ij}}\right)^{12} - 2\left(\frac{r_{IJ}}{R_{ij}}\right)^{6}\right], \tag{A1}$$

where R_{ij} is the distance between atoms i and j, D_{IJ} is the bond energy, and r_{IJ} is the equilibrium bond length:

$$r_{IJ} = \frac{1}{2}(r_{II} + r_{JJ}) \quad \text{and} \quad D_{IJ} = \sqrt{D_{II}D_{JJ}}. \tag{A2}$$

TABLE I. Values obtained here for the parameters in the potential energy term $E_{vdw}^{\mathrm{LJ6\text{-}12}}$ of Eqs. (A1) and (A2). These parameters are based on the work by Halicioglu and Pound (Ref. 15).

Atom	D_{II} (kcal/mol)	r_{II} (Å)
Na	3.1774	3.8990
Al	9.0430	2.9471
Ca	4.9586	4.0630
Ag	7.9510	2.9731
Au	10.1800	2.9678

We show in Table I the values we obtain for the metal atom parameters, and in Table II the results for the crystal structures with these values. Even if we are considering for metals only two-body potential functions we have obtained satisfactory results, as shown in Table II. Although we find differences in the absolute values for cohesive energies, results for both relative stability and lattice parameters for Na, Al, Ca, Ag, and Au metals in different allotropic forms (bcc, fcc, and hcp) are in good agreement with theoretical calculations from the literature.[35–37] At low temperature the observed experimental phase for Al, Au, Ag, and Ca is fcc, and hcp—similar to fcc with stacking faults—for Na.[35] The study of the relative stability of the different allotropic phases for Na must be considered carefully: DFT calculations using the linear muffin-tin orbital (LMTO) in the full potential version, and generalized gradient approximation (GGA) for exchange-correlation potential, lead to an energy difference $E(\mathrm{fcc})-E(\mathrm{bcc})$ of only 5 meV/atom; the same difference was obtained with LDA.[41] Calculations performed with the full potential linearized augmented plane-wave (FLAPW) method and GGA approximation show that the difference in total energy for the bcc and fcc structure is only 0.3 meV per atom at equilibrium, favoring the bcc structure.[42] This small energy difference lies within the uncertainty of the calculation, estimated to be on the order of 1 meV/atom.[42] According to Smith *et al.*,[43] the experimental observation of the

TABLE II. Cohesive energy (E_{cohe}) and equilibrium lattice parameters (a,c), for different allotropic forms of bulk metals, obtained in this work from molecular mechanics geometrical optimization with the nonbonded potential $E_{vdw}^{\mathrm{LJ6\text{-}12}}$ of Eqs. (A1) and (A2), compared to literature data.

	E_{cohe} (eV/atom)		a (Å)		c (Å)	
	This work	Ref.	This work	Ref.	This work	Ref.
			Na			
fcc	−1.160	−1.130[a]	5.360	5.337[a]		
hcp	−1.160		3.790		6.190	
bcc	−1.109	−1.130[a]	4.291	4.230[a]		
			Al			
fcc	−3.345	−4.072[b]	4.050	4.019[b]		
hcp	−3.345	−4.023[b]	2.864	2.845[b]	4.676	4.646[b]
bcc	−3.200	−3.929[b]	3.241	3.216[b]		
			Ca			
fcc	−1.805	−1.840[c]	5.587	5.586[c]		
hcp	−1.805	−1.839[c]	3.951	3.950[c]	6.456	6.450[c]
bcc	−1.725	−1.818[c]	4.471	4.365[c]		
			Ag			
fcc	−2.941	−2.950[a]	4.085	4.100[a]		
hcp	−2.940		2.889		4.717	
bcc	−2.817	−2.929[a]	3.269	3.255[a]		
			Au			
fcc	−3.765	−3.810[a]	4.078	4.090[a]		
hcp	−3.765		2.884		4.709	
bcc	−3.601	−3.763[a]	3.263	3.253[a]		

[a]Reference 35, Empirical potential.
[b]Reference 36, DFT LDA.
[c]Reference 37, Empirical potential.

TABLE III. Mean lattice parameters (in Å) and angles (in degrees) obtained from MD simulations at 300 K, using E_{vdw}^{LJ6-12} [see Eq. (A1)], in a *N-P-T* ensemble; we include also our results obtained with MM geometrical optimization of the unit cell shown in Table I, for fcc ($a=b=c$, $\alpha=\beta=\gamma=90°$), and finally the experimental data.

MM (fcc)	MD 300 K, *N-P-T*		Experimental data
		Ca	
5.587	$a=(5.67\pm0.15)$	$\alpha=(89.9\pm1.4)$	5.5884;90[a]
	$b=(5.64\pm0.17)$	$\beta=(90.1\pm1.2)$	
	$c=(5.58\pm0.23)$	$\gamma=(89.9\pm1.9)$	
		Al	
4.0496	$a=(4.07\pm0.06)$	$\alpha=(90.1\pm0.9)$	4.0495;90[b]
	$b=(4.07\pm0.05)$	$\beta=(90.0\pm1.3)$	
	$c=(4.06\pm0.06)$	$\gamma=(90.0\pm1.3)$	
		Ag	
4.0850	$a=(4.09\pm0.08)$	$\alpha=(90.0\pm1.4)$	4.0853;90[c]
	$b=(4.12\pm0.07)$	$\beta=(90.0\pm0.6)$	
	$c=(4.08\pm0.07)$	$\gamma=(90.0\pm1.5)$	
		Au	
4.0780	$a=(4.08\pm0.04)$	$\alpha=(90.0\pm0.9)$	4.0782;90[d]
	$b=(4.08\pm0.04)$	$\beta=(90.0\pm1.3)$	
	$c=(4.10\pm0.06)$	$\gamma=(90.0\pm1.3)$	

[a]Reference 17.
[b]Reference 18.
[c]Reference 19.
[d]Reference 20.

coexistence of various phases, including bcc, indicates that the energy differences should be small. In this way, we can conclude that our results for relative stabilities are satisfactory. Finally, we compare in Table III the lattice parameters obtained above with the mean lattice parameters obtained from MD simulation at 300 K in a *N-P-T* ensemble (which are of real interest to us), and again with experimental data. In all these simulations we used the force field parameters of Table I. As we can see, the force field is reproducing the experimental values for lattice parameters at 300 K.

Although the force field as developed so far is satisfactory for normal conditions, they fail when we try to reproduce the experimental *P-V* diagrams; the simulated metals are "harder" than experimentally verified. Even if for our goal here this was not mandatory, we propose also a set of parameters to be used in conjunction with a Morse-type force field, which reproduce well *P-V* diagrams and lattice constants at high pressures, as will be described next.

2. High pressure: Morse for E_{vdw}

In this case, since we have to explore different phases and pressure conditions, in order to initialize our fitting procedure we start from specific calculations for the potential energy obtained through density-functional calculations. Our DFT-LDA calculations are performed using the same meth-

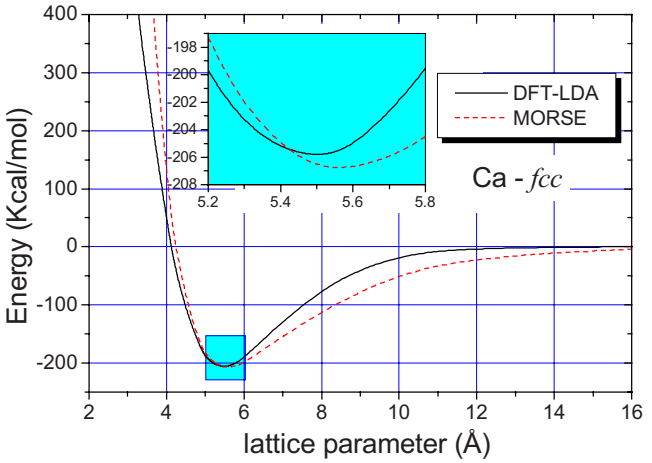

FIG. 8. (Color online) Total energy against lattice parameter for the bulk Ca metal in fcc configuration, obtained through DFT-LDA (solid black line) and MM optimization (dashed red line), as described in the text. Inset: region close to the energy minimum.

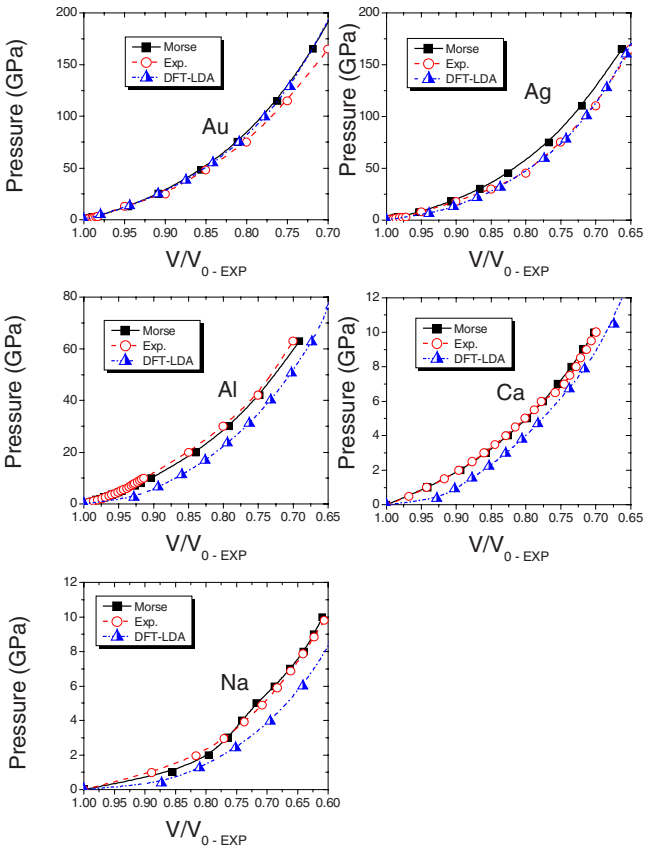

FIG. 9. (Color online) Pressure-volume diagrams for bulk metals obtained through MM unit-cell optimization using the E_{vdw}^{M} potential term of Eq. (A3) and parameters shown in Table IV (black line, squares), compared with experimental data (Ref. 45) (red line, circles) and results from DFT-LDA calculations (blue line, triangles).

TABLE IV. Parameters used in the force field for the nonbonded energy term E_{vdw}^{M} of Eqs. (A3) and (A4), suitable to reproduce geometrical features of bulk metals under pressure (see text).

Atom	D_{II} (Kcal/mol)	r_{II} (Å)	y_i
Al	6.9450	3.4050	7.1390
Ca	3.5150	5.0500	6.6500
Na	1.9500	4.7530	6.7000
Ag	10.1500	3.0840	8.9000
Au	12.1950	3.0140	9.7500

odology described above in Sec. II with a energy cutoff for plane waves of 30 hartrees and a Monkhorst-Pack[44] grid of $6\times6\times6$ in the first Brillouin zone, for bulk metals Al, Ca, Na, Ag, and Au. For each metal we realized 1SCF calculations, varying the lattice parameter, in order to obtain total energy curves as a function of lattice parameter, and the *PV* diagram for the bulk metals. The *PV* diagrams obtained from DFT-LDA show good agreement with experimental data for Au and Ag metals (see Fig. 9). For the others metals, indeed, they show a systematic error, indicative of a relatively "softer" material.

The DFT-LDA total energy curve is used as a starting choice to fit the E_{vdw} potential term. From available functionals from the OFF module,[21] we have chosen the Morse function, found to be the best choice to fit the DFT-LDA total energy curve:

$$E_{vdw}^{M} = D_{IJ}(x^2 - 2x),$$

$$x = \exp\left(-\frac{y_{IJ}}{2}\left(\frac{R_{ij}}{r_{IJ}} - 1\right)\right), \tag{A3}$$

where R_{ij} is the distance between atoms i and j, D_{IJ} is the potential energy depth in Kcal/mol, r_{IJ} is the equilibrium distance, and y_{IJ} is a parameter to adjust the rate of exponential growing. The force field parameters r_{IJ}, D_{IJ} *e* y_{IJ} are combined through

$$r_{IJ} = \frac{1}{2}(r_{II} + r_{JJ}); \quad D_{IJ} = \sqrt{D_{II}D_{JJ}}; \quad \text{and} \quad y_{IJ} = \sqrt{y_{II}y_{JJ}}. \tag{A4}$$

After the first initial fit to LDA, we proceed to adjust the parameters to the experimental data. This is detailed in Fig. 8 for the calcium metal, where we show in particular the difference in the obtained LDA lattice parameter, compared to the experimental data, and the full potential energy curves, the initial guess (LDA), and that obtained with the Morse simulation. Proceeding, we adjust the parameters to obtain the full dependence on pressure, as shown in Fig. 9, for all metals parametrized here. To do that, we optimized the unit-cell and atom positions with MM under pressure (without symmetry). The results obtained are in good agreement with experimental data. For Al, Ca and Na, we can reproduce exactly the experimental *PV* diagrams. For Au, the results are in good agreement up to a pressure of about 80 GPa; for higher pressures the simulated metal is a little "harder" than experimentally observed, but the error is small. For Ag bulk there is a systematic error of around 10% for compression above around 40 GPa, but again, this error is small. The parameters are grouped in Table IV.

TABLE V. Equilibrium lattice parameters, for bulk metals, obtained in this work from molecular mechanics unit-cell optimization with the nonbonded potential E_{vdw}^{M} of Eq. (A3) with parameters shown in Table IV.

Atom	Symmetry	Lattice parameters from (MM)	Lattice parameters (Experimental)
Al	fcc	4.0496	4.0495[a]
Ca	fcc	5.5860	5.5884[b]
Na	bcc	4.2900	4.2906[c]
Ag	fcc	4.0850	4.0853[d]
Au	fcc	4.0782	4.0782[e]

[a]Reference 18.
[b]Reference 17.
[c]Reference 46.
[d]Reference 19.
[e]Reference 20.

In order to validate the force field parameters in Table IV, we test the results for other physical properties. Initially, we performed geometrical optimization of unit-cell and atomic positions, without imposing symmetry (fcc or bcc). This allows the force field to search for the lattice parameters plus symmetry. The results of this study are shown in Table V, and are in good agreement with experimental data. We computed also the relative stability for bulk metals in different allotropic forms. The results obtained are similar to those obtained above with parameters for E_{vdw}^{LJ}. The main difference is that for Ca, Na and Ag, there is an energy difference from fcc to hcp favoring the fcc structure, and for E_{vdw}^{LJ} (Table II), for Ca and Na the energy of fcc and hcp phases are the same. We performed a last test: We used MD simulations at 300 K and 1 atm, with ensemble *N-P-T* and without symmetry for the unit cell. In this case, the results show that only for Ag and Au the unit cell is stable, keeping the fcc arrangement; for Al, Ca and Na, the unit cells deform, losing the cubic arrangement.

In summary, we conclude that the parameters in Table IV, for the E_{vdw}^{M} potential term, are suitable to describe bulk metals under pressure, while we indicate the use of E_{vdw}^{LJ} with the parameters in Table II for conditions close to normal ambient, and for the description of metallic clusters.

*Author to whom correspondence should be addressed. rgiro @if.usp.br

[1] R. H. Friend *et al.*, Nature (London) **397**, 121 (1999).
[2] P. K. H. Ho, J.-S. Kim, J. H. Burroughes, H. Becker, S. F. Y. Li, T. M. Brown, F. Cacialli, and R. H. Friend, Nature (London) **404**, 481 (2000).
[3] P. A. Lane, P. J. Brewer, J. Huang, D. D. C. Bradley, and J. C. deMello, Phys. Rev. B **74**, 125320 (2006).
[4] M. Meier, S. Karg, and W. Riess, J. Appl. Phys. **82**, 1961 (1997).
[5] J. M. Bharathan and Y. Yang, J. Appl. Phys. **84**, 3207 (1998).
[6] L. Ke, S.-J. Chua, K. Zhang, and N. Yakovlev, Appl. Phys. Lett. **80**, 2195 (2002).
[7] R. Giro and M. J. Caldas, Phys. Rev. B **76**, 161303(R) (2007).
[8] N. Koch, A. Pogantsch, E. J. W. List, G. Leising, R. I. R. Blyth, M. G. Ramsey, and F. P. Netzer, Appl. Phys. Lett. **74**, 2909 (1999).
[9] G. G. Andersson, H. H. P. Gommans, A. W. D. van der Gon, and H. H. Brongersma, J. Appl. Phys. **93**, 3299 (2003).
[10] F. J. J. Janssen, L. J. van IJzendoorn, A. W. Denier van der Gon, M. J. A. de Voigt, and H. H. Brongersma, Phys. Rev. B **70**, 165425 (2004).
[11] Y.-F. Huang *et al.*, Adv. Funct. Mater. **17**, 2902 (2007).
[12] T. Granier, E. L. Thomas, D. R. Gagnon, F. R. Karasz, and R. W. Lenz, J. Polym. Sci., Part B: Polym. Phys. **24**, 2793 (1986).
[13] A. Rappè, C. Casewit, K. Colwell, W. Goddard III, and W. Skiff, J. Am. Chem. Soc. **114**, 10024 (1992).
[14] C. J. Casewit, K. S. Colwell, and A. K. Rappé, J. Am. Chem. Soc. **114**, 10035 (1992).
[15] T. Halicioğlu and G. M. Pound, Phys. Status Solidi A **30**, 619 (1975).
[16] L. A. Girifalco and V. G. Weizer, Phys. Rev. **114**, 687 (1959).
[17] B. T. Bernstein and J. F. Smith, Acta Crystallogr. **12**, 419 (1959).
[18] W. Witt, Z. Naturforsch. A **22A**, 92 (1967).
[19] L. Liu and W. A. Basset, J. Appl. Phys. **44**, 1475 (1973).
[20] A. Maeland and T. B. Flanagan, Can. J. Phys. **42**, 2364 (1964).
[21] OFF module from CERIUS2 package, http://www.accelrys.com
[22] A. K. Rappè and W. A. Goddard, J. Phys. Chem. **95**, 3358 (1991).
[23] M. Alves-Santos, Inst. Physics University of Sao Paulo, PhD Thesis, (2008).
[24] X. Gonze *et al.*, Comput. Mater. Sci. **25**, 478 (2002).
[25] R. Bader, *Atoms in Molecules: A Quantum Theory* (Oxford University Press, New York, 1990).
[26] G. Henkelman, A. Arnaldsson, and H. Jonsson, Comput. Mater. Sci. **36**, 354 (2006).
[27] A. Kokalj, J. Mol. Graphics Modell. **17**, 176 (1999).
[28] A. Kokalj, Comput. Mater. Sci. **28**, 155 (2003).
[29] We found no significant differences for charges in the case of Na using LDA or GGA approximations (see Ref. 7), thus we adopt LDA here.
[30] S. Goedecker, M. Teter, and J. Hutter, Phys. Rev. B **54**, 1703 (1996).
[31] N. Troullier and J. L. Martins, Phys. Rev. B **43**, 1993 (1991).
[32] N. S. Murthy, R. H. Baughman, L. W. Shacklette, H. Fark, and J. Fink, Solid State Commun. **78**, 691 (1991).
[33] D. Chen, M. J. Winokur, M. A. Masse, and F. E. Karasz, Phys. Rev. B **41**, 6759 (1990).
[34] J. P. Hansen and I. R. McDonald, *Theory of Simple Liquids*, 2nd ed. (Academic, London, 1990).
[35] S. Chantasiriwan and F. Milstein, Phys. Rev. B **58**, 5996 (1998).
[36] J. C. Boettger and S. B. Trickey, Phys. Rev. B **53**, 3007 (1996).
[37] K. M. Andersson, R. L. Johnston, and J. N. Murrell, Phys. Rev. B **49**, 3089 (1994).
[38] C. Fredriksson, R. Lazzaroni, J. L. Brèdas, P. Dannetun, M. Lögdlund, and W. R. Salaneck, Synth. Met. **57**, 4632 (1993).
[39] M. Fahlman and W. R. Salaneck, Surf. Sci. **500**, 904 (2002).
[40] UNIVERSAL1.02—universal force field (UFF), available from Accelrys, Inc. as part of Materials Studio and CERIUS2 program suites. Available from http://www.accelrys.com
[41] N. E. Christensen and N. L. Novikov, Solid State Commun. **119**, 477 (2001).
[42] M. Hanfland, I. Loa, and K. Syassen, Phys. Rev. B **65**, 184109 (2002).
[43] H. G. Smith, R. Berliner, J. D. Jorgensen, and J. Trivisonno, Phys. Rev. B **43**, 4524 (1991).
[44] H. J. Monkhorst and J. D. Pack, Phys. Rev. B **13**, 5188 (1976).
[45] *American Institute of Physics Handbook*, 3rd ed., edited by D. E. Gray and B. H. Billings (McGraw-Hill, New York, 1972).
[46] E. Aruja and H. Perlitz, Z. Kristallogr. **100**, 195 (1939).